九州大学学術情報リポジトリ
Kyushu University Institutional Repository

Numerical study of infragravity waves amplification during harbor resonance

Gao, Junliang
School of Naval Architecture and Ocean Engineering, Jiangsu University of Science and Technology

Ji, Chunyan
School of Naval Architecture and Ocean Engineering, Jiangsu University of Science and Technology

Gaidai, Oleg
School of Naval Architecture and Ocean Engineering, Jiangsu University of Science and Technology

Liu, Yingyi
Research Institute for Applied Mechanics, Kyushu University

https://hdl.handle.net/2324/4055211

出版情報：Ocean Engineering. 116, pp.90-100, 2016-04-01. Elsevier
バージョン：
権利関係：Creative Commons Attribution NonCommercial NoDerivatives 4.0 International

KYUSHU UNIVERSITY

Numerical study of infragravity waves amplification during harbor resonance

Junliang Gao [a, b, c, *], Chunyan Ji [a], Oleg Gaidai [a], Yingyi Liu [d]

a School of Naval Architecture and Ocean Engineering, Jiangsu University of Science and Technology, Zhenjiang 212003, China

b Jiangsu Key Laboratory of Advanced Design and Manufacturing Technology for Ship, Jiangsu University of Science and Technology, Zhenjiang 212003, China

c Jiangsu Key Laboratory of Coast Ocean Resources Development and Environment Security, Hohai University, Nanjing 210098, China

d Research Institute for Applied Mechanics, Kyushu University, Kasuga, Fukuoka 816-8580, Japan

Abstract:

The infragravity (IG) period oscillations inside an elongated rectangular harbor excited by bichromatic wave groups are simulated using a fully nonlinear Boussinesq model. Based on an IG wave analysis technique, this study presents a comprehensive investigation on how bound and free IG waves and their relative components change with respect to the amplitudes and wavelengths of incident primary (short) waves under the condition of the lowest four resonant modes. For the given harbor and ranges of wavelength and amplitude of the primary waves studied in this paper, it is shown that the amplitudes of both the bound and free IG waves become more evident when the short wavelengths increase, and the latter are always larger than the former due to resonant amplification. The amplitudes of both the bound and free IG waves change quadratically with the amplitudes of the incident short waves.

Key Words:

Harbor resonance; Boussinesq model; Bound infragravity waves; Free infragravity waves; Wave groups

1. Introduction

Infragravity (IG) period waves are surface gravity waves with periods between 30 s and 5 min and wave lengths between 100 m and 10 km (Rabinovich, 2009). Theoretical knowledge of

the generation, propagation, dissipation and interaction of IG waves with coastlines and port structures has been highly developed since the early 1950s. Munk (1949) and Tucker (1950) carried out the first observation of the IG waves, associated with wave groups. Longuet-Higgins and Stewart (1962, 1964) determined analytical relations to explain the propagation of IG waves at wave group celerity, the genesis of bound IG wave energy and its relationship with nonlinear, spatial and temporal changes of the momentum flux of the wave trains traveling towards the shore.

When the long period waves with frequencies close to those of resonating harbor modes come into a harbor opening, they can be highly amplified into inner basins resulting in large oscillations of the water surface (Miles and Munk, 1961; Vanoni and Carr, 1950) . A variety of dynamic forcings can induce significant oscillations within a harbor. These external forcings include tsunamis originating from distance earthquake, longshore-propagating edge waves, wind and pressure fluctuations, and impact waves induced by landslides or the failure of structures near the harbor (Bellotti et al., 2012; Chen et al., 2004; De Jong and Battjes, 2004; Dong et al., 2010a). For the very long-period incident waves such as tsunamis and waves originating from wind and pressure fluctuations, they can affect only very large harbors because their natural oscillation periods are generally longer than 10 min, which matches the very long-period wave band. For most harbors around the world (where the surface water area is about 1-10 km^2 and the depth is about 5-10 m), the most common external forcing may be IG waves, mainly generated through nonlinear interaction of short wave groups. González-Marco et al. (2008) analyzed the effect of IG waves on port operations in Gijón harbor (Spain) and found that the port's inefficiency is significantly increased if IG waves are present in the wave trains, although the harbor offers very good protection against wind short waves. Similar situations can be found in various other ports and harbors around the world, such as Hua-Lien harbor in Taiwan (Chen et al., 2004), Hosojima harbor in Japan (Yoshida et al., 2000), Port of Long Beach in California (Kofoed-Hansen et al., 2005), and Pohang New Harbor in South Korea (Kumar et al., 2014). Hence, in order to identify layouts and technical solutions that minimize the downtime of the facility, it is crucial to further improve the knowledge of the IG waves inside the harbor.

The importance of incident short wave groups on IG period harbor oscillations was initially proved by Bowers (1977), both theoretically and experimentally. He studied mean free-surface oscillations in a narrow rectangular channel of constant depth and discontinuous width. A train of

sinusoidally modulated wave groups incident from infinity generates not only bound IG waves, but also additional free IG waves. Bowers (1977) demonstrated that the free IG waves are generated in the diffraction process with the same frequency as the bound IG waves because of an imbalance between the long-period fluctuations in the water pressure inside and outside the harbor entrance. This imbalance arises because the primary wave heights inside the harbor are different from the wave heights outside, giving rise to different bound IG waves inside and outside the harbor. Thus, it becomes necessary to introduce additional free IG waves for purposes of the total second-order water pressure continuity at the harbor entrance; the free IG waves will then be amplified when the group period is close to a natural period of the harbor. In the last few decades, extensive field observations and numerical simulations on IG waves inside harbors, such as Esperance harbor and Two Rocks Marina in Australia (Morison and Imberger, 1992; Thotagamuwage and Pattiaratchi, 2014a, b) , Marina di Carrarra harbor in Italy (Bellotti and Franco, 2011; Guerrini et al., 2014) , Port of Ferrol in Spain (López and Iglesias, 2013; López et al., 2012) , and Barbers Point harbor in Hawaii (Okihiro et al., 1993), have subsequently confirmed those findings by showing strong correlation between IG waves inside the harbor and short wave groups outside the harbor.

Dong et al. (2010b) implemented numerical experiments based on the Boussinesq model and employed a wavelet-based bispectrum to analyze temporary features of wave–wave interactions at various phases of IG period oscillations excited by short wave groups. The influence of short wave frequencies on IG period oscillations was also investigated in that paper. Dong et al. (2010b) found that short waves with low frequencies can excite more obvious long-period fluctuations than those with higher frequencies. The subharmonics not only get energy through difference interactions, but also export energy through sum interactions in the response and quasi-steady phases. In the damp phase, wave energy is concentrated at the lowest resonance mode, and there is a reversal energy transfer from the subharmonics to other components. Subsequently, Dong et al. (2013) proposed a wave separation procedure to decompose the IG period components inside the harbor into bound and free IG waves, and further investigated the influence of the short wavelengths on the bound and free IG waves and their relative components inside the harbor when the lowest resonant mode, which are excited by regular wave groups, occurs. For comparison, the non-resonant wave condition was also considered. Dong et al. (2013) demonstrated that the

amplitudes of bound and free IG waves and their ratio are closely related to the short wavelengths, regardless of whether the harbor is resonant or not.

To improve the understanding of the IG waves inside harbors involved in IG period oscillations, this paper further investigates how the bound and free IG waves and their relative components change with respect to the incident short waves. Compared to Dong et al. (2013), there are mainly two research developments in this paper. Firstly, in Dong et al. (2013), only the lowest resonant mode was investigated; while in this paper, we extended the resonant mode to the lowest four modes to explore the similarities and differences between different modes. Secondly, this paper systematically investigated the influence of not only the short wavelengths but also the amplitudes of the incident short waves on the bound and free IG waves and their relative components inside the harbor. In this paper, all simulations are based on the fully nonlinear Boussinesq model proposed by Wei et al. (1995). For simplification, the harbor is assumed to be long and narrow; the free surface movement inside the harbor then essentially becomes one dimensional. The water depth inside and outside the harbor is constant, and the incident waves are bichromatic with two slightly different frequencies.

The remainder of this paper is organized as follows. Section 2 describes the numerical model and the analysis technique, which will be verified using physical experimental data and known analytical signals, respectively. Section 3 presents the numerical experimental setup and the experimental wave parameters. Section 4 demonstrates the simulation results, which are explained in detail. Concluding remarks based on the results are given in Section 5.

2. Numerical model and analysis technique

2.1 Numerical model

Numerical experiments are performed using the well-known and widespread Funwave2.0 model (Kirby et al., 2003), referring to the fully nonlinear Boussinesq wave model on curvilinear coordinates. The Funwave2.0 model retains information to $O[(kh)^2]$ for frequency dispersion and to all orders for nonlinearity a/h (where k denotes the wavenumber scale, h denotes the water depth and a denotes the wave amplitude). The one-way wave maker theory proposed by Chawla and Kirby (2000) is used to generate monochromatic or random waves. Sponge layers are placed at the boundaries of the domain to effectively absorb the energy of outgoing waves with various frequencies and directions. The capability of the Funwave2.0 model to predict wave propagation

and transformation from deep to shallow water has been well validated by laboratory experiments (Bruno et al., 2009; Kirby et al., 2003).

To verify the applicability of the Funwave2.0 model to the simulation of nonlinear harbor resonance, Dong et al. (2010b) used the model to reproduce the physical experiments conducted by Rogers and Mei (1978). Dong et al. (2010b) compared the numerical results of the first three super-harmonics with the experimental data of Rogers and Mei (1978) for three long and narrow bays of different lengths. Overall agreement was observed between the measured data and the numerical results. It was demonstrated that the numerical model can also simulate nonlinear harbor resonance accurately.

2.2 Analysis technique

This paper employs the wave separation procedure originally proposed by Dong et al. (2013) to decompose the IG period components inside the harbor into bound and free IG waves. To facilitate the reader's understanding of this paper, the wave separation procedure is illustrated briefly in this section.

Fig. 1 shows the setup of the numerical experiment studied in this paper. The length of the harbor is L=100.0 m, and the width of the opening is W=5.0 m. Twenty-one wave gauges are equidistantly deployed along the central line inside the harbor; the distance between adjacent gauges, D, is equal to 5.0 m. The origin of the Cartesian coordinate system (o, x, y, z) is placed at the still water level with z measured upwards. The gauge G_{01} is installed near the inner end of the harbor; the gauge G_{21} is at the midpoint of the harbor entrance. The water depth inside and outside the harbor is constant and equal to h=2.0 m.

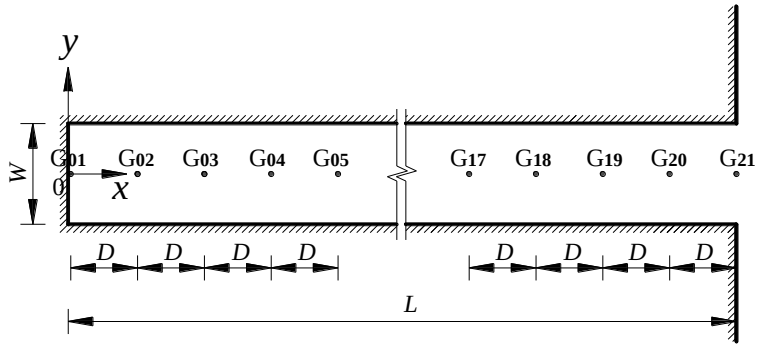

Fig. 1. Definition sketch of the harbor, the arrangement of the wave gauges and the coordinate system.

When the elongated harbor is subjected to incident bichromatic waves groups, primary waves, second-order bound and free IG waves all take the form of standing waves inside the harbor. Because of the fully reflecting vertical wall at the inner end of the harbor, an antinode exists at x=0 for all the standing wave components. Bowers (1977) has formulated these standing wave components. Following his equations, the IG period component free-surface inside the harbor can be expressed analytically as follows:

$$\eta_{\mathrm{L}}^{\mathrm{I}} = \zeta_{\mathrm{b}}^{\mathrm{I}} \cos[(2\pi\Delta f)t - \alpha_{\mathrm{b}}^{\mathrm{I}}]\cos(\Delta k x) + \zeta_{\mathrm{f}}^{\mathrm{I}} \cos[(2\pi\Delta f)t - \alpha_{\mathrm{f}}^{\mathrm{I}}]\cos(\kappa x), \tag{1}$$

where

$$\Delta f = |f_1 - f_2|, \tag{2}$$

$$\Delta k = |k_1 - k_2| \tag{3}$$

and (f_1, k_1) and (f_2, k_2) denote the frequencies and wavenumbers of the primary waves and satisfy the linear dispersion relation:

$$(2\pi f_i)^2 = gk\tanh(k_i h) \quad (i = 1, 2). \tag{4}$$

The first and second terms on the right-hand-side of Eq. (1) represent the bound and free IG standing wave components, respectively. Δf and Δk denote the frequency and wavenumber of the bound IG waves. κ denotes the wavenumber of the free IG waves, and (κ, Δf) also satisfy the linear dispersion relation. $\zeta_{\mathrm{b}}^{\mathrm{I}}$ and $\zeta_{\mathrm{f}}^{\mathrm{I}}$ denote the amplitudes of the envelop of the bound and free IG standing waves, respectively, and $\alpha_{\mathrm{b}}^{\mathrm{I}}$ and $\alpha_{\mathrm{f}}^{\mathrm{I}}$ denote the initial phases of the bound and free IG waves, respectively. The gravitational acceleration is denoted by g. Bowers (1977) noted that the second-order bound sub-harmonics contain not only the (Δf, Δk) component, but also the (Δf, k_1+k_2) component. However, calculations based on the equations in Bowers (1977) demonstrate that the (Δf, Δk) component is approximately (0.003–3.50)×10^5 times the (Δf, k_1+k_2) component in the range of our simulations (this will be described in detail in Section 3). Therefore, the (Δf, k_1+k_2) component is neglected, just as it was in Bowers (1977).

After some trigonometric manipulations, the squared amplitude of the IG period component along the central line can be expressed as follows:

$$A(x)^2 = a\varphi_0(x) + b\varphi_1(x) + c\varphi_2(x), \tag{5}$$

where

$$a=(\zeta_{\mathrm{b}}^{\mathrm{I}})^2,\ b=(\zeta_{\mathrm{f}}^{\mathrm{I}})^2,\ c=2\zeta_{\mathrm{f}}^{\mathrm{I}}\zeta_{\mathrm{b}}^{\mathrm{I}}\cos(\alpha_{\mathrm{b}}^{\mathrm{I}}-\alpha_{\mathrm{f}}^{\mathrm{I}}),$$
$$\varphi_0(x)=\cos^2(\Delta kx),\ \varphi_1(x)=\cos^2(\kappa x),\ \varphi_2(x)=\cos(\Delta kx)\cos(\kappa x). \tag{6}$$

The amplitudes of the IG period component at every gauge location, $A(x_i)$ (i=1, 2,…, 21), can be obtained using the discrete Fourier transform for the free surface signals. x_i denotes the abscissa value of each wave gauge. Because $\varphi_0(x)$, $\varphi_1(x)$ and $\varphi_2(x)$ are linearly independent, the unknown variables a, b and c can be obtained using the least squares method. Then the values of $\zeta_{\mathrm{b}}^{\mathrm{I}}$, $\zeta_{\mathrm{f}}^{\mathrm{I}}$ and $|\alpha_{\mathrm{b}}^{\mathrm{I}}-\alpha_{\mathrm{f}}^{\mathrm{I}}|$ will be obtained naturally.

It should be noted that Dong et al. (2013) just verified the capacity of this separation procedure to decompose the bound and free IG waves under the first resonant mode. However, in fact, this separation procedure can also be applied to higher resonant modes. To verify this separation procedure suitable for different resonant modes, four known analytical signals are given as follows:

$$\begin{aligned} y=&a_1^{\mathrm{I}}\cos[(2\pi f_1)t-\alpha_1^{\mathrm{I}}]\cos(k_1x)+a_2^{\mathrm{I}}\cos[(2\pi f_2)t-\alpha_2^{\mathrm{I}}]\cos(k_2x)+\\ &\zeta_{\mathrm{b}}^{\mathrm{I}}\cos[(2\pi\Delta f)t-\alpha_{\mathrm{b}}^{\mathrm{I}}]\cos(\Delta kx)+\zeta_{\mathrm{f}}^{\mathrm{I}}\cos[(2\pi\Delta f)t-\alpha_{\mathrm{f}}^{\mathrm{I}}]\cos(\kappa x), \end{aligned} \tag{7}$$

where a_1^{I} and a_2^{I} denote the amplitudes of the primary wave f_1 and f_2 components inside the harbor, respectively, and α_1^{I} and α_2^{I} denote the initial phases of the corresponding components, respectively. The first two terms represent the bichromatic short standing wave free-surfaces inside the harbor, and the third and fourth terms denote the bound and free IG standing waves inside the harbor, respectively. Table 1 presents the specific parameters of the four analytical signals. The four cases have the same wave amplitudes and initial phases for the bichromatic primary waves and the bound and free IG waves. However, the beat frequency Δf in each case is different, which is 0.010 Hz, 0.032 Hz, 0.053 Hz and 0.074 Hz in cases 01-04, respectively, corresponding to the lowest four resonant mode of the harbor illustrated in Fig. 1. This will be described in detail in Section 3. Fig. 2 shows the IG period component envelopes obtained using the known analytical signals and the separation procedure. It is obvious that there are pretty good agreements between the two curves for all the four cases. Table 2 demonstrates the amplitudes of the bound and free IG waves, the initial phase difference obtained using the separation procedure and their percentage errors relative to the known values. The percentage errors of the separating values of $\zeta_{\mathrm{b}}^{\mathrm{I}}$, $\zeta_{\mathrm{f}}^{\mathrm{I}}$ and $|\alpha_{\mathrm{b}}^{\mathrm{I}}-\alpha_{\mathrm{f}}^{\mathrm{I}}|$ relative to the known values are denoted by the terms *Err*1, 2 and 3, respectively. It is seen that all percentage errors in the four cases are less than 1.0%. Therefore,

this procedure can separate the bound and free IG standing wave components from the known analytical signals accurately for not only the first resonant mode but also the next three resonant modes when twenty-one wave gauges are installed inside the harbor.

Table 1. Parameters of four known analytic signals for testing the IG wave separation procedure

Case	f_1 (Hz)	f_2 (Hz)	a_1^{I} (m)	a_2^{I} (m)	$\zeta_{\mathrm{b}}^{\mathrm{I}}$ (m)	$\zeta_{\mathrm{f}}^{\mathrm{I}}$ (m)	α_1^{I} (°)	α_2^{I} (°)	$\alpha_{\mathrm{b}}^{\mathrm{I}}$ (°)	$\alpha_{\mathrm{f}}^{\mathrm{I}}$ (°)
01	0.200	0.210	0.05	0.05	0.01	0.02	45.0	60.0	30.0	60.0
02	0.200	0.232	0.05	0.05	0.01	0.02	45.0	60.0	30.0	60.0
03	0.200	0.253	0.05	0.05	0.01	0.02	45.0	60.0	30.0	60.0
04	0.200	0.0274	0.05	0.05	0.01	0.02	45.0	60.0	30.0	60.0

Table 2. Separation results of the bound and free IG standing waves for the four known analytical signals when twenty-one wave gauges are installed at $0 \le x \le 100$ m. *Err*1, 2 and 3 refer to the percentage errors of the separating values of $\zeta_{\mathrm{b}}^{\mathrm{I}}$, $\zeta_{\mathrm{f}}^{\mathrm{I}}$ and $|\alpha_{\mathrm{b}}^{\mathrm{I}} - \alpha_{\mathrm{f}}^{\mathrm{I}}|$ relative to the known values, respectively.

Case	$\zeta_{\mathrm{b}}^{\mathrm{I}}$ (m)	*Err*1 (%)	$\zeta_{\mathrm{f}}^{\mathrm{I}}$ (m)	*Err*2 (%)	$\lvert\alpha_{\mathrm{b}}^{\mathrm{I}} - \alpha_{\mathrm{f}}^{\mathrm{I}}\rvert$	*Err*3 (%)
01	1.000×10^{-2}	0.000	2.000×10^{-2}	0.000	30.00	0.000
02	0.999×10^{-2}	–0.100	1.998×10^{-2}	–0.100	29.96	–0.133
03	1.001×10^{-2}	0.100	2.001×10^{-2}	0.050	30.01	0.033
04	1.000×10^{-2}	0.000	2.006×10^{-2}	0.300	29.75	–0.833

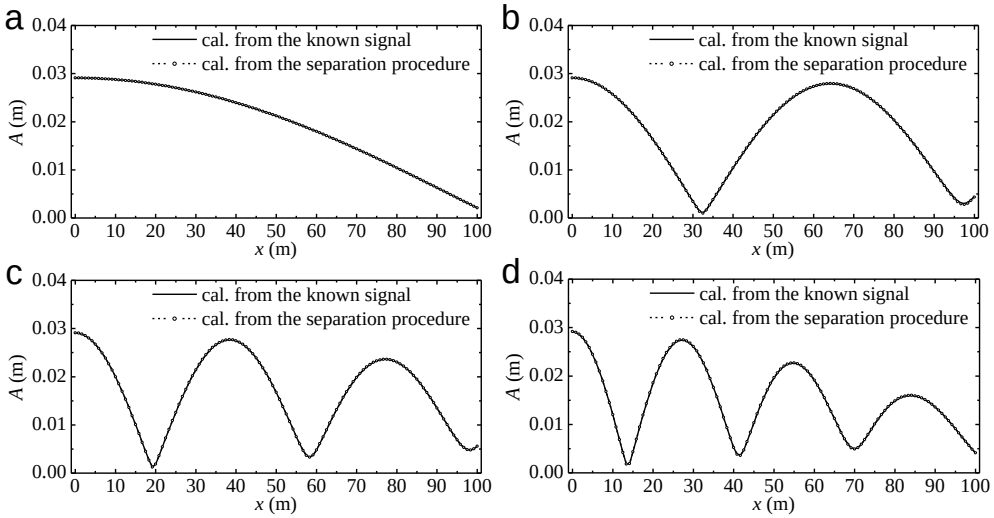

Fig. 2. The amplitude envelopes of the IG period component for the known analytical signals listed in Table 1: (a) case 01, (b) case 02, (c) case 03 and (d) case 04.

3. Numerical experiment setup

Table 3. Linear analytical solution (Mei, 1983): natural frequency, f (Hz), and amplification factor, $R(f)$, of the lowest eight resonant modes of the harbor shown in Fig. 1.

	Resonant mode							
	I	II	III	IV	V	VI	VII	VIII
f	0.010	0.032	0.053	0.074	0.095	0.116	0.137	0.156
R(f)	27.29	9.12	5.55	4.04	3.2	2.668	2.3	2.03

Using the analytical solution of the linear theory for the resonance of an elongated harbor in the absence of dissipation (Mei, 1983), the natural frequencies of the lowest eight modes of the harbor shown in Fig. 1 are calculated and listed in Table 3. This paper includes four groups of experiments, namely Groups A–D. Each group contains ten cases and has different frequency parameters. The specific parameters of all cases are listed in Table 4. Groups A–D satisfy the beat frequency Δf=0.010 Hz, 0.032 Hz, 0.053 Hz and 0.074 Hz, respectively, corresponding to the lowest four resonant modes. Although all cases in each group have the same beat frequency, the primary wave frequencies in these cases are different.

Take Group A as an example. We define $f_0=(f_1+f_2)/2$ as the average primary wave frequency for each case, and $\lambda=2\pi/k_0$ denotes the average short wavelength, in which k_0 is the wavenumber corresponding to f_0. The average primary wave frequency f_0 ranges from 0.205 Hz in case A01 to 0.385 Hz in case A10; and the average short wavelength λ varies from 20.38 m to 9.23 m accordingly. For all cases in Group A, the wavelengths of the free IG waves generated near the harbor entrance, l_f, are all equal to 442.9 m, according to the linear dispersion relation; while the wavelengths of the bound IG waves, l_b, vary from 373.0 m in case A01 to 241.6 m in case A10. In all cases, the relative water depths h/l_0 are less than 0.202; within this range, the fully nonlinear Boussinesq equations proposed by Wei et al. (1995) can be used to simulate the wave propagation and transformation accurately (l_0 denotes the deep water wavelengths of the short waves).

In order to investigate the effects of the amplitudes of the incident primary waves on the bound and free IG waves inside the harbor systematically, a total of 20 cases have been selected, in which the amplitudes of the incident primary waves, $a_1=a_2$, increased gradually from 0.005 m to 0.05 m in increments of 0.005 m. In the other cases, only the condition of $a_1=a_2$=0.05 m was

simulated. a_1 and a_2 denote the amplitudes of the incident primary wave f_1 and f_2 components, respectively.

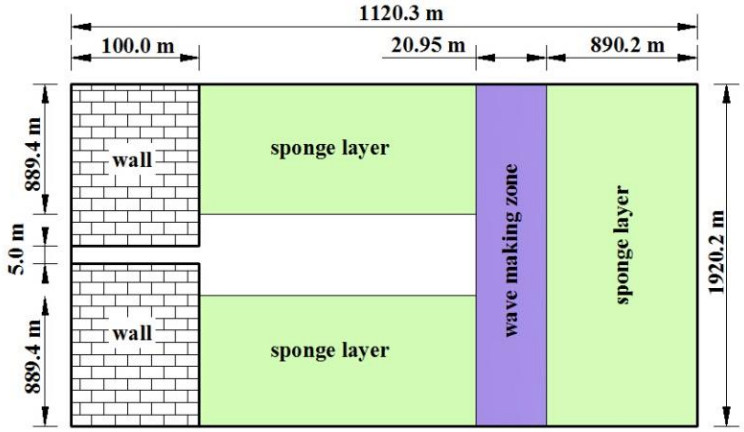

Fig. 3. Sketch of the numerical experimental setup in case A01. Based on its geometrical symmetry with respect to the *x*-axis, only half of the domain (i.e. $y \le 0$) is used as the computational domain for simulations.

Table 4. Parameters for all cases in Groups A, B, C and D. In the cases in bolds, the incident primary wave amplitudes, a_1=a_2, increased gradually from 0.005 m to 0.05 m in interval of 0.005 m; in the other cases, only a_1=a_2=0.05 m was simulated.

Group A (Δf=0.010Hz)								Group B (Δf=0.032Hz)							
Case	f_1	f_2	l_b	l_f (m)	f_0	λ (m)	h/l_0	Case	f_1	f_2	l_b	l_f (m)	f_0	λ (m)	h/l_0
A01	0.200	0.210	373.0	442.9	0.205	20.38	0.054	**B01**	0.200	0.232	114.3	138.2	0.216	19.22	0.060
A02	0.220	0.230	359.9	442.9	0.225	18.34	0.065	B02	0.220	0.252	110.1	138.2	0.236	17.36	0.071
A03	0.240	0.250	346.2	442.9	0.245	16.62	0.077	**B03**	0.240	0.272	105.7	138.2	0.256	15.78	0.084
A04	0.270	0.280	324.4	442.9	0.275	14.47	0.097	B04	0.260	0.292	101.1	138.2	0.276	14.40	0.098
A05	0.290	0.300	309.4	442.9	0.295	13.26	0.112	**B05**	0.280	0.312	96.41	138.2	0.296	13.20	0.112
A06	0.300	0.310	301.8	442.9	0.305	12.71	0.119	B06	0.300	0.332	91.65	138.2	0.316	12.14	0.128
A07	0.320	0.330	286.6	442.9	0.325	11.70	0.135	**B07**	0.320	0.352	86.88	138.2	0.336	11.19	0.145
A08	0.330	0.340	278.9	442.9	0.335	11.23	0.144	B08	0.340	0.372	82.16	138.2	0.356	10.33	0.163
A09	0.360	0.370	256.3	442.9	0.365	9.974	0.171	B09	0.360	0.392	77.52	138.2	0.376	9.558	0.181
A10	0.380	0.390	241.6	442.9	0.385	9.234	0.190	**B10**	0.370	0.402	75.25	138.2	0.386	9.198	0.191
Group C (Δf=0.053Hz)								Group D (Δf=0.074Hz)							
Case	f_1	f_2	l_b	l_f (m)	f_0	λ (m)	h/l_0	Case	f_1	f_2	l_b	l_f (m)	f_0	λ (m)	h/l_0
C01	0.200	0.253	67.63	83.26	0.227	18.20	0.066	**D01**	0.200	0.274	47.40	59.42	0.237	17.28	0.072
C02	0.220	0.273	65.02	83.26	0.247	16.50	0.078	D02	0.220	0.294	45.49	59.42	0.257	15.70	0.085
C03	0.240	0.293	62.30	83.26	0.267	15.03	0.091	**D03**	0.240	0.314	43.51	59.42	0.277	14.34	0.098
C04	0.260	0.313	59.50	83.26	0.287	13.75	0.105	D04	0.260	0.334	41.48	59.42	0.297	13.14	0.113
C05	0.280	0.333	56.64	83.26	0.307	12.63	0.120	**D05**	0.280	0.354	39.43	59.42	0.317	12.09	0.129
C06	0.300	0.353	53.77	83.26	0.327	11.62	0.137	D06	0.300	0.374	37.37	59.42	0.337	11.14	0.146
C07	0.320	0.373	50.90	83.26	0.347	10.73	0.154	**D07**	0.320	0.394	35.34	59.42	0.357	10.29	0.163
C08	0.340	0.393	48.08	83.26	0.367	9.916	0.172	D08	0.340	0.414	33.34	59.42	0.377	9.521	0.182
C09	0.350	0.403	46.69	83.26	0.377	9.540	0.182	D09	0.350	0.424	32.37	59.42	0.387	9.163	0.192

C10	0.360	0.413	45.32	83.26	0.387	9.181	0.192	**D10**	0.360	0.434	31.41	59.42	0.397	8.822	0.202

Fig. 3 illustrates the sketch of the numerical experimental setup in case A01. At the right, upper and bottom boundaries of the domain, sponge layers are installed to absorb the energy of reflected and radiated waves, and the width of the sponge layers is set to be slightly larger than 2.0 times the wavelength of the free IG waves. It should be noted that in order to reduce the computational cost, only half of the domain (i.e. $y \le 0$) is used as the computational domain for simulations based on the geometrical symmetry with respect to the *x*-axis. As the numerical model is discretized using curvilinear grids, different grid spaces are adopted. In the *x*-direction, the grid sizes Δx are all equal to 0.50 m both inside and outside the harbor except in the sponge layer at the right boundary. In order to reduce the large computational cost associated with the relatively thick sponge layer, the grid sizes Δx in the sponge layer increase gradually from 0.50 m to 10.42 m. While in the *y*-direction, the grid sizes Δy increase gradually from 0.50 m inside the harbor to 12.57 m outside the harbor. Twenty-one wave gauges are arrayed inside the harbor, and the distance between adjacent gauges is D=5.0 m. The computational domain consists of 134,300 nodes and 133,560 rectangular elements. To obtain a good convergence rate, the Courant number $Cr = \sqrt{gh}\Delta t / \min(\Delta x, \Delta y)$ should be less than 0.5. Therefore, we used a time step of Δt=0.05 s in all cases. The total simulation time was 2000 s.

4. Results and discussion

4.1 Time series and spectra analysis

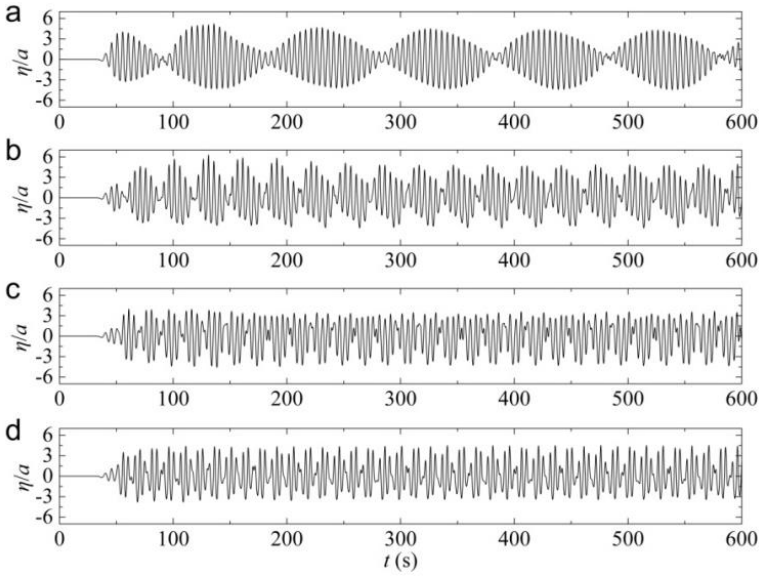

Fig. 4. Time series of the free surfaces at the gauge G_{01} for (a) case A01, (b) case B01, (c) case C01 and (d) case D01 under the condition of $a_1=a_2=0.05$ m, in which $a=(a_1a_2)^{1/2}$.

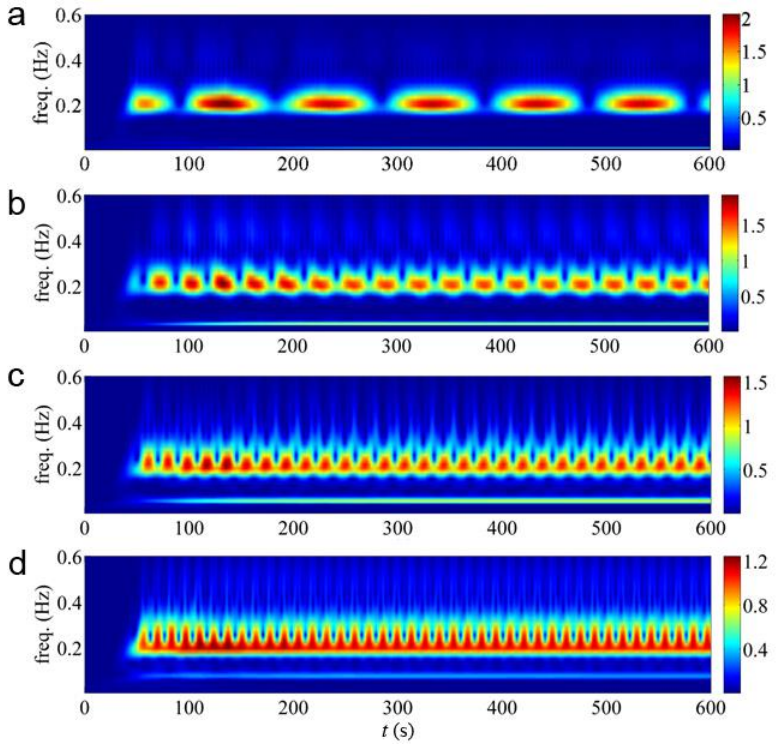

Fig. 5. Wavelet spectra at the gauge G_{01} for (a) case A01, (b) case B01, (c) case C01 and (d) case D01 under the condition of $a_1=a_2=0.05$ m.

Time series and corresponding wavelet spectra of the free surfaces at the gauge G_{01} for cases A01, B01, C01 and D01 under the condition of $a_1=a_2=0.05$ m are presented in Fig. 4 and Fig. 5, respectively. Note that in Fig. 4, the time series of the free surfaces at the gauge G_{01} are normalized by the average amplitude of the incident primary waves, $a=(a_1a_2)^{1/2}$. Fig. 4 shows that the free surface inside the harbor is calm at the initial period of time. The primary waves reach the position of gauge G_{01} at approximately 40 s for all four cases. Through the wavelet spectra illustrated in Fig. 5, the wave energy change with respect to the time and the frequency can be visually demonstrated. It is shown that the energies of the primary wave components increase from zero to their maximum levels very rapidly (about 20–40 s) and then remain relatively steady until the end of the simulations. However, more time is needed for the IG period components to attain the quasi-steady state from the initial response phase. For the four cases, it is shown that the IG period components attain the quasi-steady state at approximately 300 s. In this paper, we study

the quasi-steady processes only, in all cases.

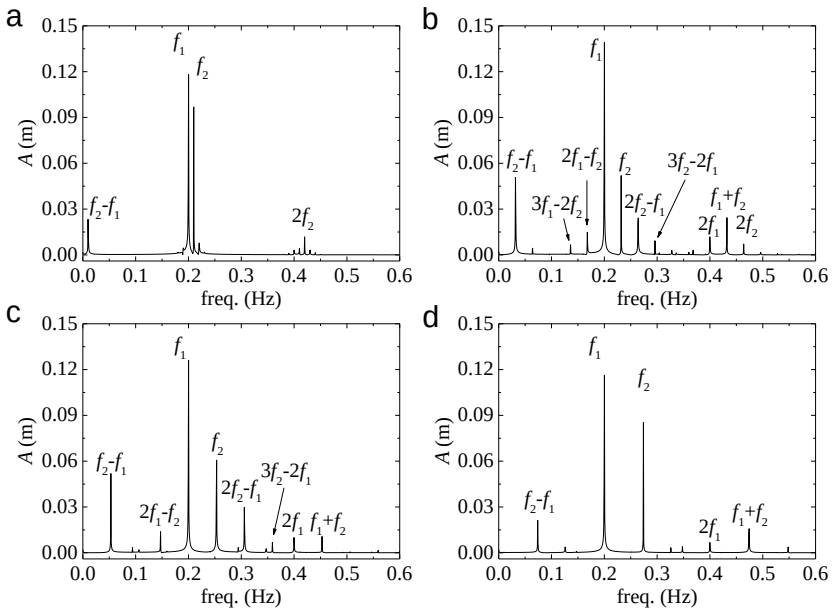

Fig. 6. Amplitude spectra at the gauge G_{01} for (a) case A01, (b) case B01, (c) case C01 and (d) case D01 under the condition of a_1=a_2=0.05 m.

During each run, data are recorded simultaneously from all gauges at a sampling time of 0.05 s, yielding 40,000 data points per gauge. After discarding the first 7,232 data points from the beginning to eliminate the effects of the initial response phase, the remaining 2^{15} data points are analyzed using a standard FFT package. The amplitude spectra at the gauge G_{01} for cases A01, B01, C01 and D01 under the condition of a_1=a_2=0.05 m are illustrated in Fig. 6. For cases B01 and C01, the nonlinear energy transfer between the primary waves and the high-order wave components are intense and complicated. Besides the primary wave f_1 and f_2 components, the amplitudes of the second- and higher-order wave components ($2f_1$, $2f_2$, f_1+f_2, f_2–f_1, $2f_1$–f_2, $2f_2$–f_1, $3f_1$–$2f_2$, $3f_2$–f_1) are also remarkable. The amplitudes of the f_2 component in these two cases are only 0.052 m and 0.061 m, respectively, much less than the values of $2a_2$, which is because there exists the notable energy transfer from the f_2 component to the second- and higher-order wave components. For the cases A01 and D01, the nonlinear energy transfer is much weaker than that in cases B01 and C01. The amplitudes of the f_1 and f_2 components in cases A01 and D01 are all close to the corresponding theoretical values of $2a_1$ and $2a_2$; in the high-order wave components, only the components $2f_1$, $2f_2$, f_1+f_2, f_2–f_1 are marked.

4.2 Effects of the short wavelength on IG waves

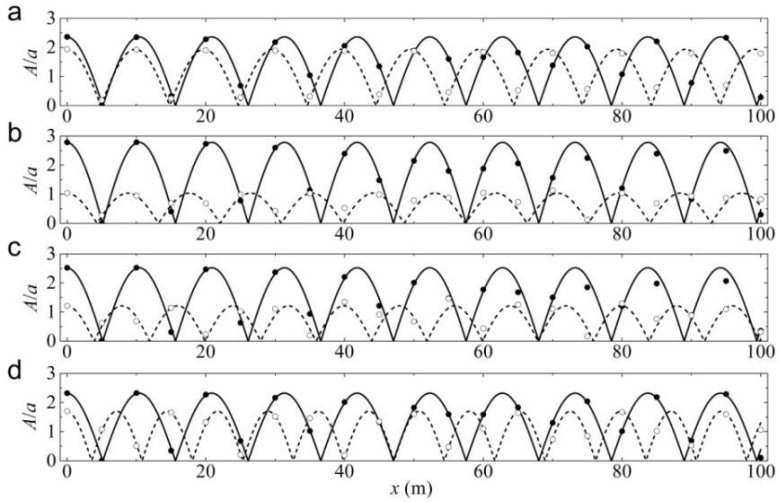

Fig. 7. Amplitudes of the primary wave f_1 and f_2 components at all wave gauges (denoted by the solid and open circles, respectively) and the corresponding theoretical envelopes (denoted by the solid and dashed lines, respectively) for (a) case A01, (b) case B01, (c) case C01 and (d) case D01 under the condition of a_1=a_2=0.05 m.

As mentioned in Section 2.2, the primary wave f_1 and f_2 components take the form of standing waves inside the harbor. According to Eq. (7), the envelops of the f_1 and f_2 components can be analytically expressed by $a_1^{\mathrm{I}}|\cos(k_1 x)|$ and $a_2^{\mathrm{I}}|\cos(k_2 x)|$, respectively, and the amplitudes of the envelopes, a_1^{I} and a_2^{I}, can be obtained using the discrete Fourier transform for the free surface signals at the gauge G_{01}. Fig. 7 illustrates the comparisons of the amplitudes of the f_1 and f_2 components at all wave gauges extracted from the corresponding free surface signals and their theoretical envelopes for cases A01, B01, C01 and D01 under the condition of a_1=a_2=0.05 m. It is shown that there is good agreement between the extracted amplitudes and the theoretical envelopes for all the four cases, which illustrates that the primary wave components inside the harbor are simulated by the numerical model accurately.

Using the separation procedure based on the discrete Fourier transform and the least squares method proposed in Section 2.2, the bound and free IG standing waves inside the harbor are separated in all cases. Fig. 8 shows the amplitudes of the IG period components in all wave gauges and their envelopes obtained using the separation procedure for cases A01, B01, C01 and D01

(where A_{IG} denotes the amplitude of the IG period components). It can be shown that the amplitudes of the IG period components at all wave gauges are very close to their envelopes in all the four cases. The separation results of the four cases are listed in Table 5. For the four cases, although the values of A_{IG}, ζ_b^I and ζ_f^I are different from each other, the values of ζ_b^I / ζ_f^I are all less than 100%. This indicates that the relative components of the bound IG waves are less than those of the free IG waves inside the harbor.

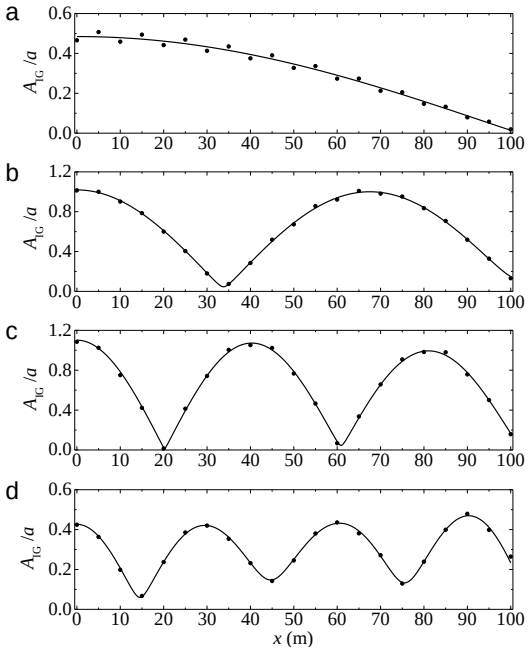

Fig. 8. Amplitudes of the IG period components (dots) at all wave gauges and their envelopes (solid lines) obtained using the separation procedure for (a) case A01, (b) case B01, (c) case C01 and (d) case D01 under the condition of a_1=a_2=0.05 m.

Table 5. The separation results of the bound and free long wave components for cases 01A, 01B, 01C and 01D under the condition of a_1=a_2=0.05 m.

Case	ζ_b^I (m)	ζ_f^I (m)	$\lvert \alpha_b^I - \alpha_f^I \rvert$	ζ_b^I / ζ_f^I (%)
A01	1.14×10^{-2}	1.29×10^{-2}	11.07^o	88.37
B01	8.94×10^{-3}	4.63×10^{-2}	63.39^o	19.31
C01	7.37×10^{-3}	4.82×10^{-2}	22.75^o	15.29
D01	7.93×10^{-3}	2.14×10^{-2}	101.49^o	37.06

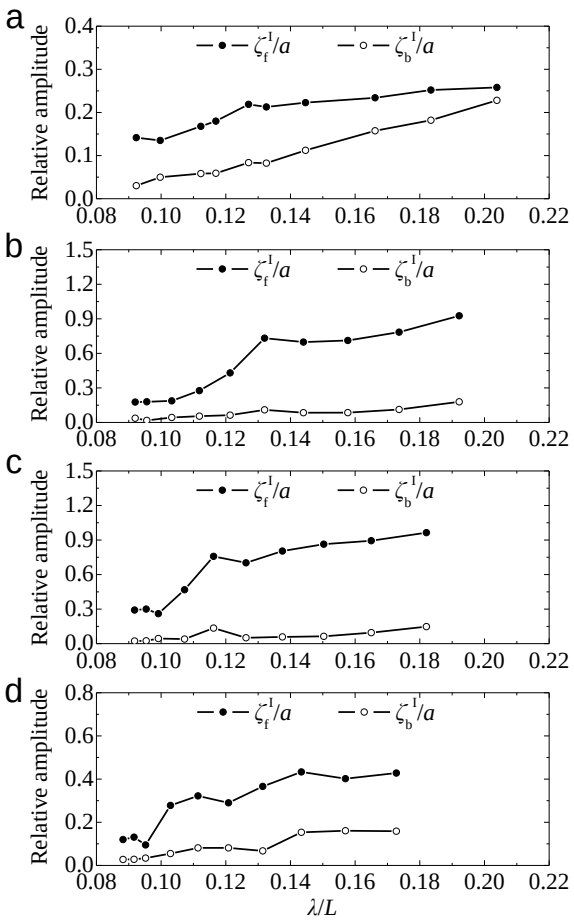

Fig. 9. The separating amplitudes of the bound and free IG waves for all cases in (a) Group A, (b) Group B, (c) Group C and (d) Group D under the condition of a_1=a_2=0.05m.

Fig. 9 shows the variation of the amplitudes of bound and free IG waves with respect to the wavelengths of the incident primary waves in Groups A, B, C and D under the condition of a_1=a_2=0.05m. For both the bound and free IG waves, it is obvious that their amplitudes are more evident when the short wavelengths are relatively large. These phenomena coincide with the findings in Dong et al. (2013), and the reasons about these phenomena have been interpreted qualitatively from the standpoints of the nonlinear triad interactions and the generation mechanism of the free IG waves in Dong et al. (2013). Besides, we can see that for all the four groups, the amplitudes of the free IG waves are always larger than those of the bound IG waves inside the harbor, which is due to that the free IG waves in the four groups correspond to the lowest four resonant modes, respectively, and were significantly amplified inside the harbor. To better show the difference and resemblance between the lowest four resonant modes, Fig. 10 demonstrates the comparisons of the amplitudes of the bound and free IG waves in Groups A-D under the condition

of a_1=a_2=0.05m. It is interesting that both the magnitude and changing trend of the amplitudes of the bound IG waves in the four groups are very close to each other. However, the amplitudes of the free IG waves in the four groups are different with each other. Overall, the amplitudes of the free IG waves in Groups B and C are apparently larger than those in Groups A and D. Therefore, it can be inferred that for the primary wave frequency ranges studied in this paper, the overall IG waves under the second and third modes are more notable than those under the lowest mode, which breaks the usual stereotype that for narrow-mouthed bays and harbors, as well as for narrow elongated inlets and fjords, the lowest mode normally dominates (Rabinovich, 2009).

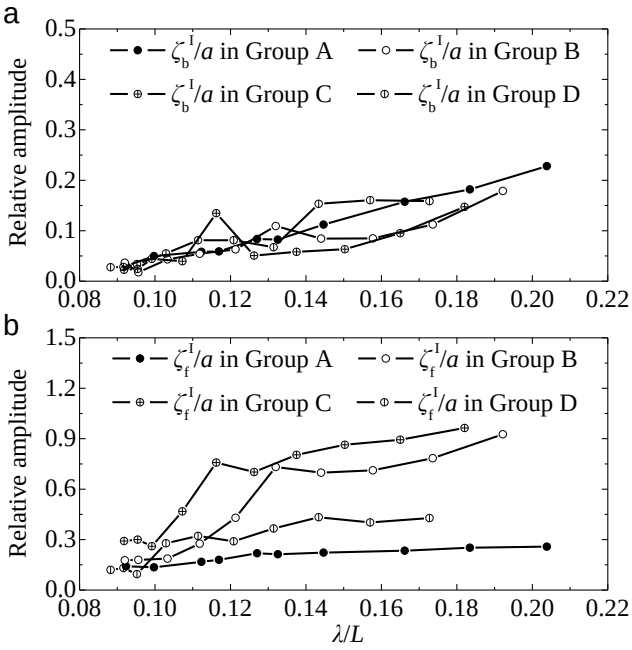

Fig. 10. Comparisons of the separating amplitudes of the bound and free IG waves in Groups A-D under the condition of a_1=a_2=0.05m: (a) the bound IG waves and (b) the free IG waves

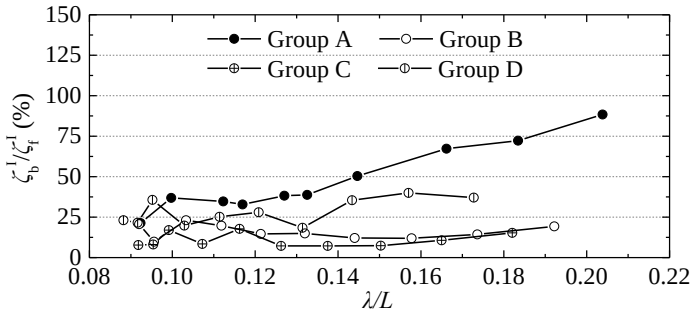

Fig. 11. The amplitude ratios, ζ_b^I / ζ_f^I, for all cases in Groups A-D under the condition of a_1=a_2=0.05m.

Fig. 11 illustrates the variation of the amplitude ratio, ζ_b^I / ζ_f^I, with respect to the short wavelengths in Groups A–D under the condition of a_1=a_2=0.05m. Because the free IG wave components are always larger than the bound IG wave components inside the harbor, the value of ζ_b^I / ζ_f^I in all cases are less than 100%. For the first mode (Group A), when the normalized short wavelength λ/L is larger than 0.144, the values of ζ_b^I / ζ_f^I are always larger than 50% and increase gradually with the increase of λ/L; when the normalized short wavelengths λ/L is less than 0.133, the amplitude ratio ζ_b^I / ζ_f^I fluctuates in the range of 20–40%. For the second and third mode (Groups B and C), the values of ζ_b^I / ζ_f^I vary only between 5% and 25%, which is less than those in the lowest mode overall. For the fourth mode (Group D), the amplitude ratio ζ_b^I / ζ_f^I changes in the range of 20–40%, which in general falls in between the first mode and the second and third modes.

4.3 Effects of the short wave amplitude on IG waves

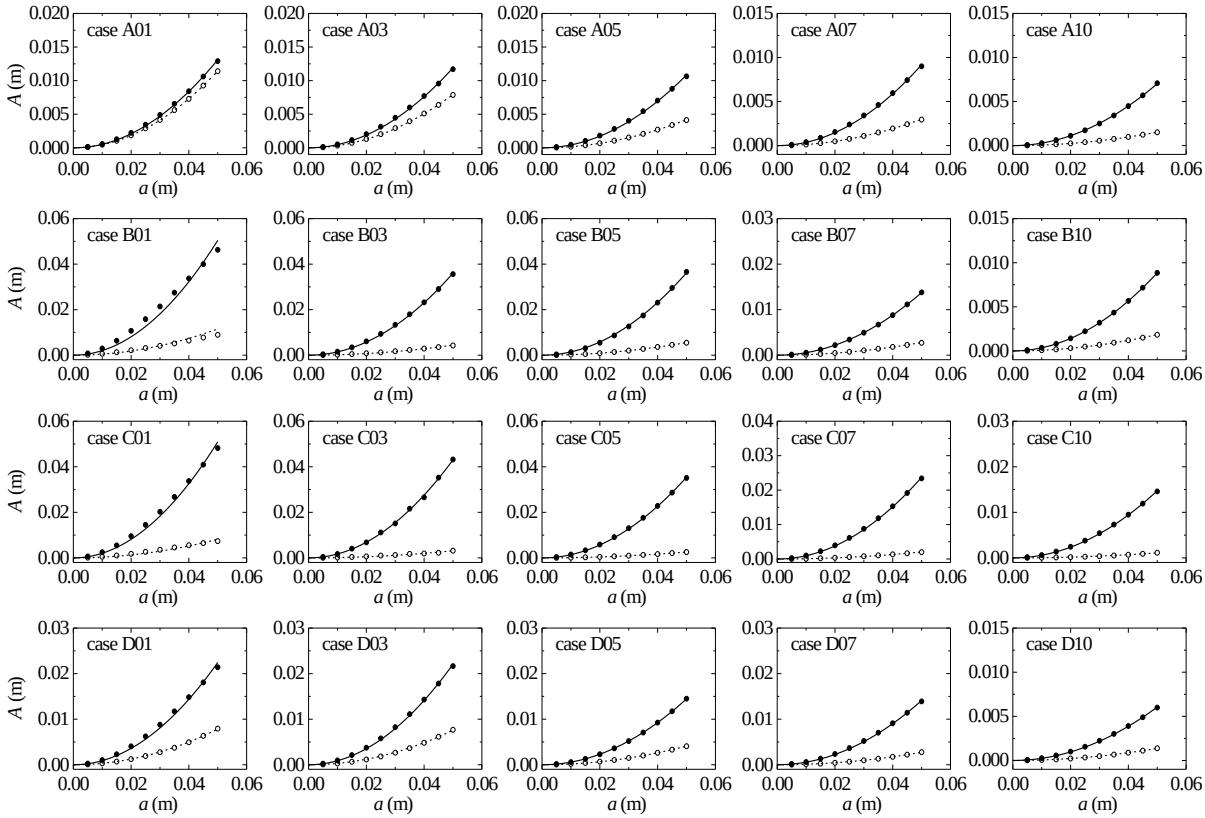

Fig. 12. Variation of the amplitudes of the bound and free IG waves, $\zeta_{\mathrm{b}}^{\mathrm{I}}$ and $\zeta_{\mathrm{f}}^{\mathrm{I}}$, with respect to the average amplitude of the incident primary waves, *a*. The open and solid circles denote the separating amplitudes of the bound and free IG waves, $\zeta_{\mathrm{b}}^{\mathrm{I}}$ and $\zeta_{\mathrm{f}}^{\mathrm{I}}$, respectively; and the dashed and solid curves denote the corresponding fitted amplitudes by Eq. (8).

Fig. 12 shows the variation of amplitudes of the bound and free IG waves, $\zeta_{\mathrm{b}}^{\mathrm{I}}$ and $\zeta_{\mathrm{f}}^{\mathrm{I}}$, with respect to the average amplitude of the incident primary waves, *a*, for the cases in bold in Table 4. It can be observed intuitively that the separating amplitudes of the bound and free IG waves, $\zeta_{\mathrm{b}}^{\mathrm{I}}$ and $\zeta_{\mathrm{f}}^{\mathrm{I}}$, seem to change quadratically with the amplitudes of the incident primary waves. To test the idea, it is assumed that there exist the following functional relations between the amplitudes of the bound and free IG waves and the amplitudes of the incident primary waves:

$$\begin{cases} \zeta_{\mathrm{b}}^{\mathrm{I}} = \nu_{\mathrm{b}} a^2 \\ \zeta_{\mathrm{f}}^{\mathrm{I}} = \nu_{\mathrm{f}} a^2 \end{cases}, \tag{8}$$

where ν_{b} and ν_{f} are unknown coefficients, which can be determined by using the least squares method. Table 6 presents the values of the parameters ν_{b}, ν_{f} and the correlation coefficients R^2 in

these cases. It can be seen that the correlation coefficient R^2 are all larger than 0.99 except in cases B01, B03 and C01. However, the values of R^2 in the latter three cases are also larger than 0.96. It demonstrates that the bound and free IG wave components inside the harbor indeed vary quadratically with the amplitudes of the incident primary waves.

Table 6. Values of the parameters v_b, v_f and the correlation coefficient R^2

Case	ζ_b^I		ζ_f^I		Case	ζ_b^I		ζ_f^I	
	v_b	R^2	v_f	R^2		v_b	R^2	v_f	R^2
A01	4.572	0.9999	5.245	0.9992	B01	3.880	0.9729	20.18	0.9740
A03	3.175	0.9996	4.763	0.9988	B03	1.767	0.9753	14.41	0.9995
A05	1.673	0.9996	4.339	0.9991	B05	2.221	0.9996	14.49	0.9994
A07	1.197	0.9997	3.673	0.9990	B07	1.115	0.9985	5.503	1.000
A10	0.6093	0.9998	2.812	0.9999	B10	0.7434	0.9992	3.541	1.000
C01	3.278	0.9634	20.38	0.9912	D01	3.125	0.9995	8.981	0.9940
C03	1.253	0.9946	17.22	0.9991	D03	3.029	0.9995	8.832	0.9989
C05	1.035	0.9989	14.18	0.9997	D05	1.636	0.9998	5.787	1.000
C07	0.8205	0.9968	9.485	0.9995	D07	1.092	0.9998	5.642	0.9995
C10	0.4411	0.9983	5.893	0.9997	D10	0.5496	0.9999	2.422	0.9997

According to Longuet-Higgins and Stewart (1962, 1964), the amplitude of the bound IG waves generated through the wave-wave nonlinear interaction is proportional to the square of the amplitudes of the primary waves. Therefore, in theory, the amplitude of the bound IG waves inside the harbor, ζ_b^I, is proportional to $(a^I)^2$, where $a^I = (a_1^I a_2^I)^{1/2}$ denotes the average amplitudes of the primary waves inside the harbor. The amplitudes of the primary standing waves inside the harbor, a_1^I and a_2^I, can be obtained using the discrete Fourier transform for the free surface signals at the gauge G_{01} in each case (refer to Fig. 7). Then the value of a^I in each case can be calculated naturally. Fig. 13 illustrates the variation of the average amplitudes of the primary waves inside the harbor, a^I, with respect to the average amplitude of the incident primary waves, a. Assuming that a^I is proportional to a, that is,

$$a^I = \gamma a. \tag{9}$$

Using the least square method, the coefficient γ for each case can be obtained (see Table 7). It can be observed that the correlation coefficient R^2 are all larger than 0.99 except in cases B01, B03 and C01, in which R^2 are also larger than 0.96. It proves that a^I is indeed proportional to a.

Therefore, the reason why the bound IG wave components inside the harbor, ζ_b^I, vary quadratically with the amplitudes of the incident primary waves, a, can be explained well. We have noticed that the fitting results for cases B01, B03 and C01 are not very perfect in comparison with other cases especially when a is large (see Figs. 12 and 13). It is probably due to that the notable energy transfer from the f_2 component to the second- and higher-order wave components occurs in the three cases (see Fig. 6. The amplitude spectrum for case B03, not shown in the paper, is similar to those for cases B01 and C01).

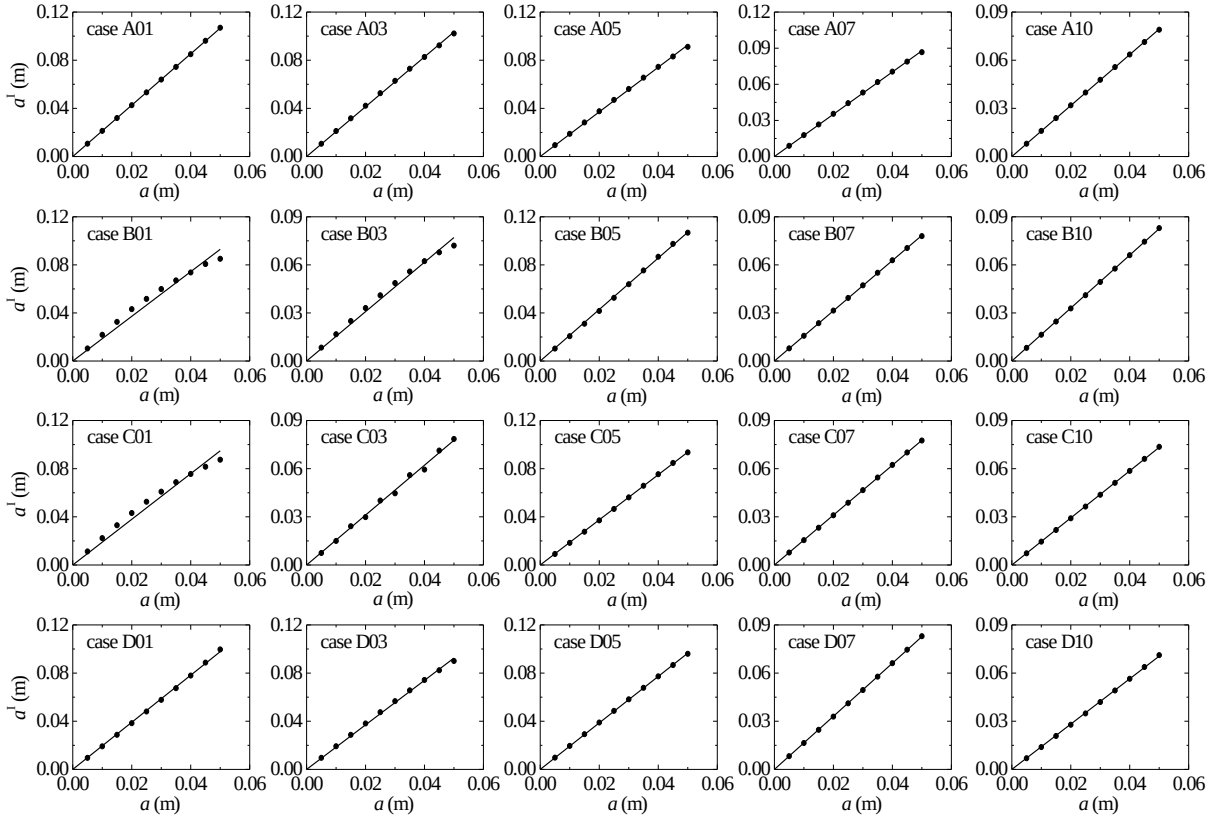

Fig. 13. Variation of the average amplitudes of the primary waves inside the harbor, a^I, with respect to the average amplitude of the incident primary waves, a. The solid circles refer to the calculated a^I, and the solid lines denote the corresponding fitted a^I by Eq. (9).

Table 7. Values of the parameter γ and the correlation coefficient R^2

Case	γ	R^2	Case	γ	R^2	Case	γ	R^2	Case	γ	R^2
A01	2.133	1.000	B01	1.859	0.9670	C01	1.897	0.9701	D01	1.956	0.9991
A03	2.069	0.9994	B03	1.541	0.9875	C03	1.554	0.9959	D03	1.849	0.9980
A05	1.854	0.9993	B05	2.143	0.9993	C05	1.875	0.9998	D05	1.931	0.9999
A07	1.756	0.9996	B07	1.568	0.9999	C07	1.554	1.000	D07	1.654	1.000
A10	1.588	0.9999	B10	1.652	0.9999	C10	1.466	0.9999	D10	1.411	0.9997

The reason why the free IG wave components inside the harbor change quadratically with the amplitudes of the incident primary waves, a, can be qualitatively explained through the generation mechanism of the free IG waves near the harbor mouth. According to Longuet-Higgins and Stewart (1962, 1964), the amplitudes of the bound IG waves outside the harbor, $\zeta_{\mathrm{b}}^{\mathrm{E}}$, is proportional to a^2, that is,

$$\zeta_{\mathrm{b}}^{\mathrm{E}}=\psi a^2, \tag{10}$$

in which $\psi=\psi(f_1, f_2, h)$. Based on the generation mechanism of the free IG waves (Bowers, 1977), the free IG wave components inside the harbor can be qualitatively expressed as follows:

$$\zeta_{\mathrm{f}}^{\mathrm{I}}=R\left|\zeta_{\mathrm{b}}^{\mathrm{I}}-\zeta_{\mathrm{b}}^{\mathrm{E}}\right|=R\left|\nu_{\mathrm{b}}-\psi\right|a^2=R\delta a^2, \tag{11}$$

in which R denote the amplification factor, related to the resonant mode. Because the primary wave heights inside the harbor are different from the wave heights outside, there exists an imbalance between the bound IG waves inside and outside the harbor (Bowers, 1977). Thus, the coefficient $\delta=\left|\nu_{\mathrm{b}}-\psi\right|\neq 0$. Based on the results shown in Fig. 12 and Table 6, it can be found that for the given water depth, ν_{b} in Eq. (8) is only a function of the variables f_1 and f_2. Therefore, for the given water depth, δ is also only a function of the variables f_1 and f_2, unrelated to the primary wave amplitudes. Further, for the specific resonant mode and primary wave frequencies, the value of $R\delta$ becomes a constant, and $\zeta_{\mathrm{f}}^{\mathrm{I}}$ varies quadratically with a.

Fig. 14 illustrates the variation of the amplitude ratios, $\zeta_{\mathrm{b}}^{\mathrm{I}}/\zeta_{\mathrm{f}}^{\mathrm{I}}$, with respect to the average amplitude of the incident primary waves, a. It can be found intuitively that when the lowest four modes occur inside the harbor, the amplitude ratio in each case are only slightly affected by the amplitudes of the incident primary waves. The maximum variations of $\zeta_{\mathrm{b}}^{\mathrm{I}}/\zeta_{\mathrm{f}}^{\mathrm{I}}$ in Groups A-D occur in cases A01, B01, C02, and D01, respectively. For the four cases, the amplitude ratios vary

in the ranges of 81.00–88.37%, 18.66–21.14%, 6.40–10.59% and 30.16–37.06, respectively.

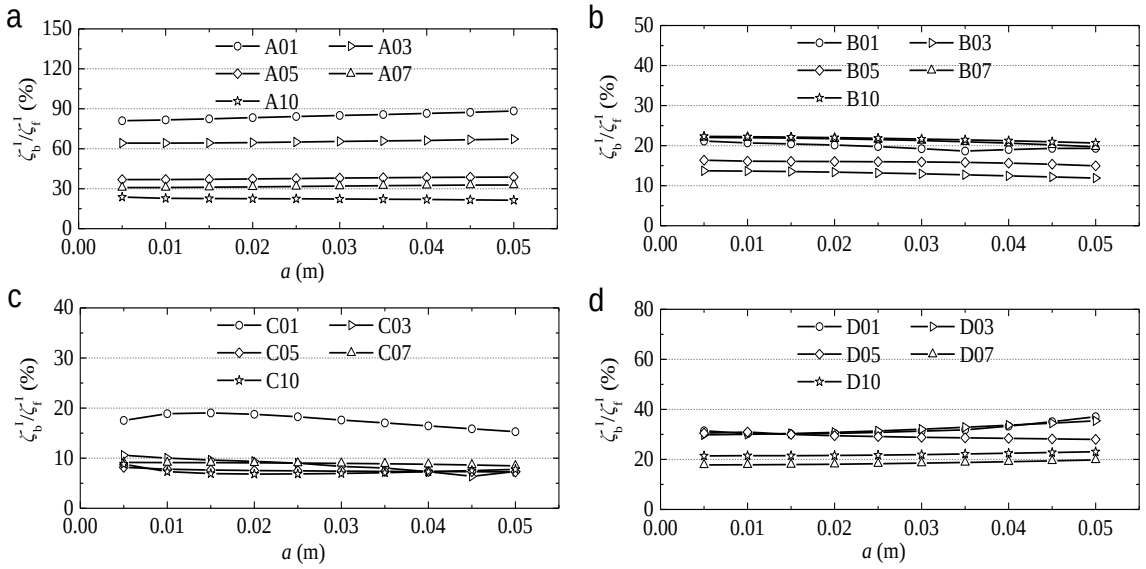

Fig. 14. Variation of the amplitude ratios, ζ_b^1/ζ_f^1, with respect to the average amplitude of the incident primary waves, *a*, in (a) Group A, (b) Group B, (c) Group C and (d) Group D

5. Conclusion

The harbor oscillations under the lowest four modes induced by bichromatic wave groups were simulated using the fully nonlinear Boussinesq model. The variations of the bound and free IG waves inside the harbor and their ratio relative to the wavelengths and amplitudes of the incident primary (short) waves were investigated systematically. The similarities and differences between the lowest four modes were also presented in this study. It is hoped that the results of this study will improve the understanding of IG waves inside harbors involved in IG period oscillations.

Our simulations found that both the bound and free IG waves inside the harbor are closely related to the wavelengths and amplitudes of the incident primary waves under the lowest four resonant modes. Both the bound and free IG wave components become more evident as the short wavelength increases. Because the frequencies of the free IG waves generated near the entrance correspond to the lowest four resonant modes, they are amplified inside the harbor, and their amplitudes are always larger than those of the bound IG waves. For the primary wave frequency ranges studied in this paper, the bound IG wave components under the lowest four modes have a

similar magnitude and changing trend to each other; the free IG waves under the second and third modes are apparently larger than those under the lowest mode. Therefore, the overall IG waves under the second and third modes are more notable than those under the lowest mode. However, the amplitude ratios under the former two modes are less than those under the latter overall. Furthermore, it was also found that both the bound and free IG waves inside the harbor vary quadratically with the amplitudes of the incident primary waves. However, the amplitude ratios of them, ζ_b^I / ζ_f^I, are only slightly affected by the short wave amplitudes.

Finally, we reaffirm here that these conclusions are only valid for the given harbor and the ranges of the wavelength and amplitude of the primary waves studied in this paper. The energy dissipation due to the flow separation near the entrance and wave breaking may markedly change the distribution and strength of the low-frequency component inside the harbor. These processes were not considered in the current study.

Acknowledgements

This work was financially supported by the National Natural Science Foundation of China (Grant Nos. 11172058, 51221961, 51422901) and the Jiangsu Key Laboratory of Coast Ocean Resources Development and Environment Security (Grant No. JSCE201508) .

References

Bellotti, E.C., Franco, L., 2011. Measurement of long waves at the harbor of Marina di Carrara, Italy. Ocean Dynamics 61 (12), 2051-2059.

Bellotti, G., Briganti, R., Beltrami, G.M., 2012. The combined role of bay and shelf modes in tsunamis amplification along the coast. Journal of Geophysical Research 117, C08027, doi: 10.1029/2012JC008061.

Bowers, E.C., 1977. Harbour resonance due to set-down beneath wave groups. Journal of Fluid Mechanics 79, 71-92.

Bruno, D., Serio, F.D., Mossa, M., 2009. The FUNWAVE model application and its validation using laboratory data. Coastal Engineering 56 (7), 773-787.

Chawla, A., Kirby, J.T., 2000. A source function method for generation of waves on currents in Boussinesq models Applied Ocean Research 22 (2), 75-83.

Chen, G.-Y., Chien, C.-C., Su, C.-H., Tseng, H.-M., 2004. Resonance induced by edge waves in Hua-Lien harbor. Journal of Oceanography 60, 1035-1043.

De Jong, M.P.C., Battjes, J.A., 2004. Seiche characteristics of Rotterdam Harbour Coastal Engineering 51 (5-6), 373-386

Dong, G., Gao, J., Ma, X., Wang, G., Ma, Y., 2013. Numerical study of low-frequency waves during harbor resonance. Ocean Engineering 68, 38-46.

Dong, G., Wang, G., Ma, X., Ma, Y., 2010a. Harbor resonance induced by subaerial landslide-generated impact waves. Ocean Engineering 37 (10), 927-934.

Dong, G., Wang, G., Ma, X., Ma, Y., 2010b. Numerical study of transient nonlinear harbor resonance. Science China-Technological Sciences 53, 558-565.

González-Marco, D., Sierra, J.P., Ybarra, O.F.d., Sánchez-Arcilla, A., 2008. Implications of long waves in harbor management: The Gijón port case study. Ocean & Coastal Management 51 (2), 180-201.

Guerrini, M., Bellotti, G., Fan, Y., Franco, L., 2014. Numerical modelling of long waves amplification at Marina di Carrara Harbour. Applied Ocean Research 48, 322-330.

Kirby, J.T., Long, W., Shi, F., 2003. Funwave 2.0 Fully Nonlinear Boussinesq Wave Model On Curvilinear Coordinates. Center for Applied Coastal Research Dept. of Civil & Environmental Engineering, University of Delaware, Newark.

Kofoed-Hansen, H., Kerper, D.R., Sørensen, O.R., Kirkegaard, J., 2005. Simulation of long wave agitation in ports and harbours using a time-domain Boussinesq model, Proceedings of the Fifth International Symposium on Ocean Wave Measurement and Analysis (WAVES), Madrid, Spain.

Kumar, P., Zhang, H., Kim, K.I., 2014. Spectral Density Analysis for Wave Characteristics in Pohang New Harbor. Pure and Applied Geophysics 171, 1169-1185.

López, M., Iglesias, G., 2013. Artificial intelligence for estimating infragravity energy in a harbor. Ocean Engineering 57, 56-63.

López, M., Iglesias, G., Kobayashi, N., 2012. Long period oscillations and tidal level in the Port of Ferrol. Applied Ocean Research 38, 126-134.

Longuet-Higgins, M.S., Stewart, R.W., 1962. Radiation stress and mass transport in gravity waves, with application to 'surf beat'. Journal of Fluid Mechanics 13 (4), 481-504

Longuet-Higgins, M.S., Stewart, R.W., 1964. Radiation stresses in water waves ; a physical discussion, with applications. Deep-Sea Research 11, 529-562.

Mei, C.C., 1983. The Applied Dynamics of Ocean Surface Waves. Wiley, New York.

Miles, J., Munk, W., 1961. Harbor paradox. Journal of the Waterways and Harbors Division 87, 111-132.

Morison, M.L., Imberger, J., 1992. Water-Level Oscillations in Esperance Harbour. Journal of Waterway, Port, Coastal, and Ocean Engineering 118 (4), 352-367.

Munk, W.H., 1949. Surf beats. Eos, Transactions American Geophysical Union 30 (6), 849-854.

Okihiro, M., Guza, R.T., Seymour, R.J., 1993. Excitation of Seiche Observed in a Small Harbor. Journal of Geophysical Research 98 (C10), 18,201-218,211.

Rabinovich, A.B., 2009. Seiches and harbor oscillations, in: Kim, Y. (Ed.), Handbook of Coastal and Ocean Engineering. World Scientific Publishing, Singapoure, pp. 193-236.

Rogers, S.R., Mei, C.C., 1978. Nonlinear resonant excitation of a long and narrow bay. Journal of Fluid Mechanics 88 (1), 161-180.

Thotagamuwage, D.T., Pattiaratchi, C.B., 2014a. Influence of offshore topography on infragravity period oscillations in Two Rocks Marina, Western Australia. Coastal Engineering 91, 220-230.

Thotagamuwage, D.T., Pattiaratchi, C.B., 2014b. Observations of infragravity period oscillations in a small marina. Ocean Engineering 88, 435-445.

Tucker, M., 1950. Surf beats: sea waves of 1 to 5 min. period. Proceedings of the Royal Society of London. Series A, Mathematical and Physical Sciences. 202 (1071), 565-573.

Vanoni, V.A., Carr, J.H., 1950. Harbor surging, Proceedings of the 1st International Conference on Coastal Engineering, Long Beach, pp. 60-68.

Wei, G., Kirby, J.T., Grilli, S.T., Subramanya, R., 1995. A fully nonlinear Boussinesq model for surface waves. Part 1. Highly nonlinear unsteady waves. Journal of Fluid Mechanics 294, 71-92.

Yoshida, A., Murakami, K., Uchida, M., Irie, I., 2000. Long period water surface oscillations and ship motions in Hosojima Harbor, Proceedings of the 27th International Conference on Coastal Engineering American Society of Civil Engineers, Sydney, Australia, pp. 3655-3668.